

LA-UR-24-23103

Accepted Manuscript

Inferring fusion nuclear burnwidths with low gain photomultiplier impulse response functions

Meaney, Kevin Daniel; Jeet, Justin; Carrera, J. A.; Mariscal, E.; Schlossberg, D. J.; Moore, A. S.; Eckart, M.; Miles, J; Hink, P; Hillyard, Patrick W.; Holdener, D.; Geppert-Kleinrath, Hermann; Kim, Yong Ho

Provided by the author(s) and the Los Alamos National Laboratory (2025-01-15).

To be published in: Review of Scientific Instruments

DOI to publisher's version: 10.1063/5.0213471

Permalink to record:














<https://permalink.lanl.gov/object/view?what=info:lanl-repo/lareport/LA-UR-24-23103>



Los Alamos National Laboratory, an affirmative action/equal opportunity employer, is operated by Triad National Security, LLC for the National Nuclear Security Administration of U.S. Department of Energy under contract 89233218CNA000001. By approving this article, the publisher recognizes that the U.S. Government retains nonexclusive, royalty-free license to publish or reproduce the published form of this contribution, or to allow others to do so, for U.S. Government purposes. Los Alamos National Laboratory requests that the publisher identify this article as work performed under the auspices of the U.S. Department of Energy. Los Alamos National Laboratory strongly supports academic freedom and a researcher's right to publish; as an institution, however, the Laboratory does not endorse the viewpoint of a publication or guarantee its technical correctness.

RESEARCH ARTICLE | DECEMBER 02 2024

Inferring fusion nuclear burnwidths with low gain photomultiplier impulse response functions

K. D. Meaney ; J. Jeet ; J. Carrera ; E. Mariscal ; D. Schlossberg ; A. Moore ; M. Eckart ; J. Milnes ; P. Hink ; P. Hillyard; D. Holdener ; H. Herrmann ; H. Geppert-Kleinrath ; Y. Kim 



Rev. Sci. Instrum. 95, 123501 (2024)

<https://doi.org/10.1063/5.0213471>



View
Online



Export
Citation

Articles You May Be Interested In

KoopmanLab: Machine learning for solving complex physics equations

APL Mach. Learn. (September 2023)

Experimental realization of a quantum classification: Bell state measurement via machine learning

APL Mach. Learn. (September 2023)



Special Topics Open for Submissions

[Learn More](#)

Inferring fusion nuclear burnwidths with low gain photomultiplier impulse response functions

Cite as: Rev. Sci. Instrum. 95, 123501 (2024); doi: 10.1063/5.0213471

Submitted: 10 April 2024 • Accepted: 6 November 2024 •

Published Online: 2 December 2024



View Online



Export Citation



CrossMark

K. D. Meaney,^{1,a)} J. Jeet,² J. Carrera,² E. Mariscal,² D. Schlossberg,² A. Moore,² M. Eckart,² J. Milnes,³ P. Hink,³ P. Hillyard,⁴ D. Holdener,⁴ H. Herrmann,¹ H. Geppert-Kleinrath,¹ and Y. Kim¹

AFFILIATIONS

¹ Los Alamos National Laboratory, Los Alamos, New Mexico 87545, USA

² Lawrence Livermore National Laboratory, Livermore, California 94550, USA

³ Photek Ltd, 26 Castleham Road, Hastings, St Leonards on Sea East Sussex, TN38 9NS, United Kingdom

⁴ Nevada Nuclear Security Site, Lawrence Livermore Operations, 161 S. Vasco Road, Ste A, Livermore, California 94551, USA

^{a)} Author to whom correspondence should be addressed: meaney@lanl.gov

ABSTRACT

When an inertial confinement fusion implosion is compressed, it maintains thermonuclear density and temperatures for a very short time scale, about 100 ps. The Gamma Reaction History diagnostic measures the time evolution of the fusion burn, but its temporal resolution is limited by the use of a photomultiplier tube (PMT) to amplify the photon signal. Multichannel plate-based PMTs have a fast (~120 ps) full-width at half-max impulse response function (IRF), but the time scale is similar to the incoming physics signal. An analysis routine is used to remove the effect of the PMT IRF and infer the incident fusion burnwidth. With the National Ignition Facility achieving ignition and creating much brighter signals, the PMTs are run at gains three orders of magnitude lower than nominal operation. Calibration at these settings shows the PMT IRFs get ~15% wider. Taking the gain-dependent IRF can affect the inferred nuclear burnwidths by up to ~15%.

© 2024 Author(s). All article content, except where otherwise noted, is licensed under a Creative Commons Attribution (CC BY) license (<http://creativecommons.org/licenses/by/4.0/>). <https://doi.org/10.1063/5.0213471>

I. INTRODUCTION

In inertial confinement fusion (ICF), a capsule filled with deuterium-tritium (DT) fuel is compressed to high temperatures and densities, creating thermonuclear conditions. The time scales of thermonuclear burn are very short, with the nuclear fusion emission varying from 50 to 200 ps.

Measuring the time evolution of the fusion reaction, the reaction history, is a powerful constraint on the energy balance of the fusion hotspot. The full-width-at-half-max (FWHM) of the reaction history is called the burnwidth. The burnwidth, τ_{BW} , is one of the values for calculating the spatially and temporally averaged DT yield, $\overline{Y_{DT}}$, in addition to the number density of deuterium n_D and tritium n_T , the volume V , and the Boltzmann-averaged cross-section $\langle\sigma v\rangle$,

$$\overline{Y_{DT}} \approx n_D n_T \langle\sigma v\rangle V \tau_{BW}. \quad (1)$$

The burnwidth is related to the deceleration time of an ICF capsule,¹ is related to the thermodynamic conditions approaching stagnation,² is used as a metric to estimate the isobaric pressure near stagnation,³ and is used to tune and compare with ICF simulations. For ICF, the nuclear burnwidth is also related to the fusion triple product—the hotspot pressure times the confinement time, $P\tau$, which estimates the nuclear performance. The nuclear burnwidth is distinct from the confinement time,^{4–6} but 1D hydrodynamic simulations have suggested that they are proportional.⁷ The burnwidth is also a metric of compression of the implosion, which is stable across the transition to ignition.⁸

Experimentally, the reaction history is measured with the Gamma Reaction History (GRH) diagnostic at the National Ignition Facility (NIF) and OMEGA laser facility.^{9–11} The DT fusion reaction creates a rare ~15 MeV gamma ray that can be used as a direct probe of the fusion reaction history—as gamma rays have no temporal broadening due to the Doppler effect, unlike

particles with mass, like the DT neutrons. The GRH uses the Cherenkov mechanism through a pressurized gas cell to allow for energetic isolation of the DT fusion gamma rays, only measuring photons with energies >10 MeV. As the DT fusion gamma rays hit the detector, they create Compton electrons that fly into the pressurized gas. The electrons, going faster than the speed of light in the gas cell, create Cherenkov radiation that is collected with parabolic mirrors and focused onto a photomultiplier (PMT). The Cherenkov mechanism is also fast—the dispersion of Cherenkov light taking various optical paths has about an 8 ps impulse response function (IRF). ICF creates a strong radiation pulse, with many collected photons in a very short amount of time ($>10^4$ to 10^8 photons in 100 ps), requiring running the PMTs in the current mode. The number of Cherenkov photons collected needs to be amplified for a large enough signal to be recorded onto a digitizer. The temporal bottleneck of the GRH detector has been the PMT, specifically the amplification technique.

PMTs are used across a wide set of applications as a valuable diagnostic tool for amplifying photon signals.^{12–14} PMTs have a photocathode, converting the incoming photons to electrons, followed by multiple stages with a high voltage. The potential accelerates the electrons, which strike a stage, creating an avalanche of more electrons that continue through other stages, amplifying the initial electron signal. The IRF of a PMT depends on the dispersion of different trajectories the electrons take as they flow through the amplification process. To achieve a fast (<500 ps) IRF requires a micro-channel plate (MCP)-based PMT^{15–17} as opposed to dynode-based PMTs, which have typical IRF of nanoseconds. An MCP uses thin disks of photoelectric material with narrow pores. The small variation in the possible electron paths, and, therefore, transit time, through the pores of the MCP creates a fast instrument response. Photek Ltd. manufactures MCP PMTs designed for a fast IRF, the fastest of which uses an anode diameter of 10 mm with either one or two stages of MCPs, with the FWHM of the IRF around ~ 100 ps or ~ 120 ps,^{18,19} a max gain of $\sim 10^4$ or 10^6 , respectively, and a charge limit of around 1.2 nC.²⁰ The GRH uses Photek 10 mm PMTs for its photon amplification, with the IRF of the full GRH system dominated by the IRF of the PMT.²¹

The precise details of the PMT IRF are important for reconstructing the reaction history. As an example, if the incoming physics fusion reaction history signal of ~ 130 ps is convolved with the GRH system IRF, giving a measured signal of ~ 170 ps. Both a forward fit and deconvolution routine are applied to remove the effect of the PMT to infer the width of the incident physics signal. In realistic data, the deconvolution and forward fit are only able to infer the width of the incoming signal if it is near or wider than the width of the PMT IRF. Specific details of the PMT IRF, such as the ringing structure, frequency spectrum, and measured noise on both the IRF and the physics signal, are important to how well one can reconstruct the incoming signal, specifically limiting how narrow an incoming signal can be reconstructed.

Furthermore, although not focused in detail in this paper, the quartz Cherenkov detectors' (QCD) neutron time-of-flight diagnostics used at both NIF and OMEGA similarly uses fast IRF PMTs. Neutron time-of-flight detectors are located far (~ 20 m) from the implosion. As the DT fusion neutrons fly away from the ICF implosion, the neutron pulse broadens as different neutrons

have different velocities due to downscattering and thermal Doppler broadening. With the knowledge of the distance of the detector from the implosion, the time of arrival of the neutron corresponds to the energy of the neutron. The IRF of the PMT broadens the neutron arrival time, which translates into a broadening of the measured neutron energy spectrum.^{22,23} These QCD detectors use extremely precise timing to make precise downscattered neutron measurements to observe asymmetries.²⁴ In the QCD diagnostic as well, the details of the IRF are important to remove the instrument response to accurately reconstruct the neutron spectrum. Historically, an average representative IRF for a PMT was used for data analysis.

Recently, the NIF has achieved ignition, increasing nuclear fusion yield performance significantly and increasing the resulting signal levels drastically.^{25,26} The gain of the PMT is dependent on the bias voltage applied to the MCP. Each PMT has a unique max bias and an operational range of voltage to be applied to the MCP. For PMTs used in the GRH, the manufacturer-supplied bias voltage range spans a range of typically 0.8 kV, for example, a PMT may have a reported bias range from 4.8 to 4 kV. This bias range typically gives a gain range of $100\times$ (10^4 to 10^2) for a single MCP and $1000\times$ for a two-stage MCP (10^6 to 10^3). However, with extremely bright signals, the gain had to be reduced further, and therefore, the applied biases decreased well below the 0.8 kV range provided. For the highest yield ICF implosions achieved so far, gain values of 10 or lower are needed, requiring the applied voltage to be typically 2 kV lower than the maximum voltage, well beyond the standard manufacturer-supplied bias voltage range. Similarly, the QCD had to turn the gain of the PMT to very low settings.

At these low applied bias voltages, there was uncertainty in how the gain dependence varies, how the IRF varies, and whether gain stability, i.e., applied gain for the same input signal, is maintained. Data were collected across a set of 15 single- and double-stage PMTs at the short pulse laser lab located at the Nevada Nuclear Security Site (NNSS) near Lawrence Livermore National Lab. A 2 ps width laser was used to measure relative gain, IRF, and gain stability across applied bias settings on the PMT. Five PMTs were measured in very low-bias settings. In addition, four of the PMTs had a modified design incorporating a Zener diode, changing the characteristics of the PMT, and showing a similar dynamic range of gain (10^4 to 1) within a smaller bias voltage range of about a kV. The IRF becomes wider as gains go lower—about 20% as wide as the nominal IRF. The gain stability remains similar. Furthermore, PMTs with a Zener diode show a smaller IRF (~ 90 ps) with a wide gain dynamic range with a smaller bias range. These calibration results allow gain-specific IRFs to be used for burnwidth analysis, especially for low-bias settings of fast PMTs, and provide data for useful gain sensitivity across a few more orders of magnitude.

Taking into account the measured gain-dependent IRF improves the similarity of the result from a forward fit and a deconvolution, bringing independent measurements closer into agreement. For specific cases, such as very narrow measurements, not using the gain-dependent IRF can erroneously overestimate the width of the physics signal by about $\sim 15\%$. Going forward, the improved IRFs will be used as part of the analysis technique.

II. INFERRING NUCLEAR BURNWIDTHS

The GRH measures the time evolution of fusion emission from an imploded capsule, which has nuclear burnwidths for high-yield implosions typically varying from 50 to 150 ps. This signal propagates through the GRH detector and is convolved with the gas cell IRF (FWHM ~ 8 ps) and the PMT IRF response, which both broaden the signal. The measured signal is the convolution of the incident physics signal of the GRH instrument IRF.

An analysis routine is used to infer the incident physics signal by removing the effect of the instrument IRF. To first order, the convolution of two Gaussians results in another Gaussian with a standard deviation that is quadrature sum of the two, i.e., using dummy variables,

$$A_1 e^{-\frac{(x-\mu_1)^2}{2\sigma_1^2}} \otimes A_2 e^{-\frac{(x-\mu_2)^2}{2\sigma_2^2}} = A_3 e^{-\frac{(x-(\mu_1+\mu_2))^2}{2(\sigma_1^2+\sigma_2^2)}}. \quad (2)$$

Therefore, if the peaks are roughly Gaussian, the FWHM of incident nuclear burnwidth should go roughly as

$$\tau_{BW} \approx \sqrt{\tau_{Measured}^2 - \tau_{PMT\ IRF}^2 - \tau_{Gas\ IRF}^2}. \quad (3)$$

However, the actual fusion reaction history has skew and structure that depart from a Gaussian, and the PMT IRF has a slightly non-Gaussian peak and additional ringing structure, as shown in Fig. 1. These different functional forms depart from the idealized Gaussian quadrature scaling.

Two analysis routines are run to infer the incident burnwidth. First, the problem is solved directly by applying a general time-domain deconvolution, as described in Refs. 27 and 28. For time-domain deconvolution, a Fourier transform of the signal $S_{Measured}(t)$ is divided by the Fourier transform of the GRH system IRF $S_{IRF}(t)$, a frequency filter $F(\omega)$ is applied, and then an inverse Fourier transform is taken,

$$S_{in}(t) = \text{invFT} \left(\frac{\text{FT}(S_{Measured}(t))}{\text{FT}(S_{IRF}(t))} * F(\omega) \right). \quad (4)$$

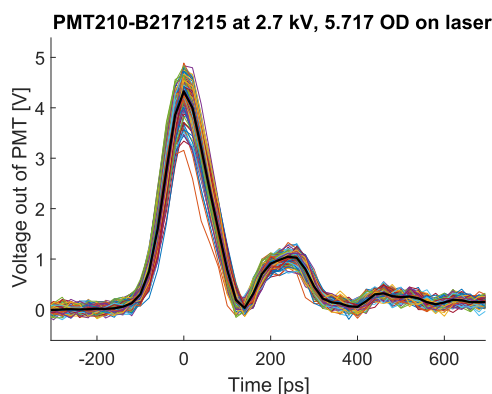


FIG. 1. Example of one collection of PMT data from 200 laser pulses. The dataset is for PMT210-B2171215 at a 2.7 kV bias (low compared to the max of 4.7 kV) with a total of 5.717 (2.717 selected +3) OD filtering. The multiple traces show the variation observed. An average of the 200 pulses is shown by a thicker black line.

The GRH deconvolution uses the Nahman–Guillaume Optimum Filter, which uses an adaptive filter that minimizes the imaginary component that is returned by the final inverse Fourier transform, as energy in the imaginary portion is non-physical and considered to be an error. This time-domain deconvolution is completely general, making no assumption about the shape of the incident physics signal. However, the ability to reconstruct the incoming signal is dependent on how precisely the frequency spectrum of both the reaction history signal and the PMT IRF is measured and further limited by the spectrum of noise on both signals. For as-measured NIF data quality and noise levels, the time-domain deconvolution can successfully infer the incoming signal to around the FWHM of the PMT IRF. For incident signals narrower than the PMT IRF, the deconvolution continues to return the width of the IRF, leveling off at a floor.

A second analysis technique is to complete a forward fit, which assumes a functional form of the incoming signal—GRH uses a skew Gaussian assumption using a Gaussian rise and a Gaussian fall with different standard deviations. The forward fit varies with the parameters of the functional form (the rising and falling standard deviation), convolves many forms with the PMT IRF, and selects the parameters that provide the best fit to the data. The forward-fit technique assumes a functional form for the incident signal but effectively fits or smooths the data that minimize the effect of noise and are less sensitive to the frequency spectrum of the peaks. The forward-fit technique is observed to be able to reconstruct the incoming width of the reaction history to around $\sim 0.9 * \text{IRF}$. For the first ignition shot on NIF, N210808, the forward fit returned and inferred a 90 ps burnwidth¹⁰ for a 100 ps PMT IRF, one of the narrowest yet observed at that time. That 90 ps burnwidth value was confirmed through a faster pulse-dilation measurement.

The GRH has four gas cells, labeled A, B, C, and D, all identical to each other but ran on different settings for each NIF implosion. One cell of GRH has recently been upgraded with a pulse-dilation PMT system. The pulse-dilation system uses a drift tube to physically stretch out the photo-electron bunch before amplification on the MCP.^{29,30} Then, this applies the ~ 100 ps IRF to a signal that is $10\times$ or $20\times$ wider. For example, a 150 ps reaction history is then effectively measured as a 1.5 ns signal, where a 100 ps MCP IRF becomes negligible. The pulse-dilation system is intended to measure fusion reaction history widths down to 10 ps, as well as allows verification of the reconstruction techniques used with the standard, slower PMTs. However, for very narrow gamma-ray signals, a deconvolution or forward fit will need to be incorporated into the pulse-dilation analysis again. For example, it is expected that as ICF performance increases and achieves extremely robust ignition, burnwidths are simulated to become as narrow as ~ 15 ps.⁸ In addition, MeV photon emission from NIF's short pulse laser Advanced Radiographic Capability (ARC) platform also have emission widths of around ~ 15 ps.²¹

III. FAST PMT CALIBRATION

A. Calibration setup

To calibrate the IRF of the PMTs, they are brought to the NNSS Livermore site short pulse laser lab, which has a Ti:Sapphire-based laser system with 400 nm wavelength, 10 Hz rep rate, and ~ 2 ps pulse

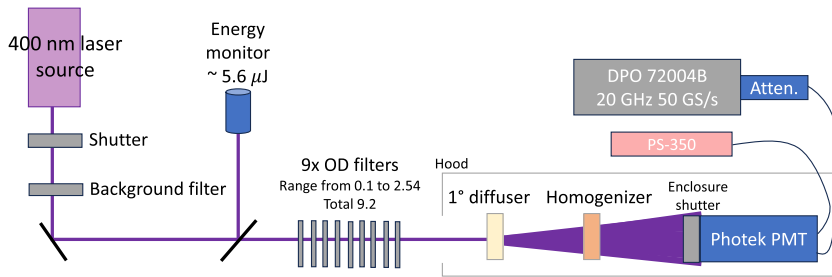


FIG. 2. Cartoon layout of the short pulse laser lab, not to scale.

width with an energy per pulse of up to 3 mJ. As the laser beam travels toward the PMT, it transits through: (1) a background filter, (2) a small percentage is reflected to an energy monitor, (3) a set of selectable optical density (OD) filters, (4) a diffuser, (5) homogenizer, and finally (6) a fixed three OD filter. The diffuser expands the spot size and the homogenizer creates a uniform illumination profile that overfills the 10 mm diameter photocathode. The OD system has a set of nine automatically individually selectable OD filter. The filters have various attenuation factors ranging from 0.01 to 2.5, with a total attenuation factor of 9.2 when all filters are in the line, plus three from the fixed OD. The OD filters are used to change the incident laser flux onto the PMT to output a few volts for a given bias setting. A high voltage power supply, (PS-350), applies voltage to the PMT and the output of the PMT has a 40 GHz cable attached to a 20 GHz Tektronix 72004B Digital Phosphor Oscilloscope with 50 giga-sample/s (10 ps per point) rate. Electronic attenuators were sometimes additionally used. The laser range setup is shown in Fig. 2. The OD filters were varied along with the gain of the PMT to measure the impulse response and the signal across a wide range for the set of PMTs.

A set of 15 Photek PMTs,³¹ manufactured between 2009 and 2022 intended for use for the GRH and QCD diagnostics were calibrated at the short pulse laser lab at various times between 2018 and 2023. Note that these PMTs are driven with negative voltages, but throughout this manuscript, it is neglected for simplicity. For these PMT designs, the MCP thickness is 0.2 mm, the pore diameter is 3 μm, and the pore bias angle is 16°. The PMTs have internal divider chains that set the voltages on the photocathode, MCP input, and MCP output, while the anode is at virtual ground. The standard PMT uses resistors across the MCP and between the MCP and the anode. In this standard configuration, changing the total voltage on the MCP to adjust the gain will also change the voltage between the MCP and the anode. Four of the PMTs incorporate a Zener diode between photocathode and MCP, instead of a resistor, thus fixing the voltage between the photocathode and MCP voltage when changing the gain. These have the effect of having a more sensitive gain for the applied bias on MCP, meaning that a change in bias has a larger gain difference on the Zener diode. This appears as a sharper slope on the gain vs applied bias plot. Both double-stage and single-stage PMTs have the same total space envelope. Table I shows the PMTs,

TABLE I. Summary of the 15 PMTs, in order of manufacture date, including whether they have a Zener diode, when they were calibrated, where fielded, what bias range they were calibrated, their FWHM, and gain for the max bias. The stability is the signal variation observed, which may be due to input laser or gain variation.

PMT serial	Zener	Calibration	Fielded	Bias range calibrated (kV)	FWHM@max bias (ps)	Gain@max bias	Stability (%)
210-73090416		2018	GCD @ OMEGA	3.45–4.8	129 ± 6	1.5 * 10 ⁶	10
210-26091009		2018	GCD @ OMEGA	3.5–5	136 ± 7	1.8 * 10 ⁶	11
110-72101208	Yes	2018	NIF GRH C before March '13	4.55–4.95	106 ± 3	4.7 * 10 ³	6
210-83150626		2018	NIF GRH A Sept '18 to Oct '21	3.95–4.55	142 ± 10	1.4 * 10 ⁶	14
110-B5160910		2020	NIF GRH B, since the April '21	2.1–4.6	101 ± 2	7.2 * 10 ³	93
110-B5170629		2019	NIF GRH B Apr '19 to Apr '22	3.7–4.6	101 ± 2	8.8 * 10 ³	17
110-13170822		2019	NIF GRH C Apr '19 to Apr '22	3.6–4.4	105 ± 2	1.0 * 10 ⁴	17
110-B5160910		2018	NIF GRH B, since the Apr '21	3.45–4.8	102 ± 2	7.2 * 10 ³	10
110-B2171215		2020	NIF GRH A, since the Jan '22	2.3–4.7	120 ± 3	8.9 * 10 ⁴	9
110-B5180105		2020	NIF GRH C, since the Apr '21	2.1–4.7	108 ± 2	1.2 * 10 ⁴	11
110-B4180202	Yes	2018	NIF GRH D Nov '18 to Nov '21	4.5–4.8	92 ± 2	7.5 * 10 ³	6
210-52180614		2020	Not fielded (backup)	2.6–4.7	208 ± 22	9.0 * 10 ⁵	11
110-B3190416	Yes	2022	Intended for QCD	4.0–4.8	102 ± 2	5.6 * 10 ⁴	...
110-B4190416	Yes	2022	Intended for QCD	4.2–4.8	98 ± 3	5.0 * 10 ⁴	...
110-B4221212		2023	QCD Alcove Testbed	2.1–4.1	111 ± 3	3.0 * 10 ⁴	...

their serial number, the year of calibration, and a summary of calibration data. For all the PMTs, a bias range is taken for around 1 kV lower than the maximum voltage. For six PMTs (two 210 s, four 110 s), the bias voltage is decreased to 2.5 kV lower than the maximum voltage. At the lowest bias voltages, there were ~4.4 OD filters (1.4 placed, 3 fixed) inline. This level of laser energy was chosen to be the maximum due to concerns about burning or damaging the PMT.

Data from 200 laser pulses are taken at each setting, with a ladder approach used by first decreasing the bias by 0.1 kV, taking data, removing some OD filters, taking data and then repeating. This often leads to two data points at a given bias, although for some specific bias settings, there are multiple data points. As part of the calibration procedure, a 10 min warm-up time was given for each PMT and the first setting was double-checked later—no deviation was observed.

B. PMT data analysis

For each bias and OD filter setting, 200 laser pulses are collected. The data are inverted to make it positive, aligned for the maximum value and a few pulses disregarded—occasional mistriggers or signals clipping. The resulting curves are averaged point by point to produce an average IRF for those settings. An example of a dataset of 200 points is shown in Fig. 1. The second peak after the primary peak is a ringing structure present in the IRF. These PMTs use anode masks, which are physical structures that limit the electron trajectories, to make the ringing pattern consistent and independent of the illumination pattern.¹⁸ The FWHM and integral

of the peaks are taken for each curve. The uncertainty of the FWHM and integral is estimated by the standard deviation of the observed FWHM and integral across the 200 shots.

The typical value from the integral across the dataset is ~1 V * ns. To calculate the gain the PMT is applying, each signal is corrected by any optical filter in place (with $I = I_0 e^{-OD/10}$). The energy monitor also measures the average laser energy before and after the 200 laser samples, varying by 1% or 2% across a dataset and up to 15% over the whole collection time of a PMT (a day). The integral is then scaled by the relative difference of the laser power drift. The integral is then converted to a relative gain by the ratio of the integral to the incident signal. Because of the effect of the energy monitor, the diffuser, the homogenizer, the overfilling of the PMT, and other effects, the absolute flux incident on the PMT is unknown. Instead, the relative gain is scaled to best match the supplied manufacturer gain values near the max voltage.

C. PMT calibration results

The dependence of the FWHM as a function of the applied bias voltage is shown in Fig. 3. Almost all the PMTs follow a similar pattern; an exception is PMT210-52180614, which has both the largest FWHM and the largest variation across bias settings. Similarly, PMT210-83150626 observes a larger-than-average variation. Each PMT has a different natural FWHM due to the manufacturing differences of specific MCPs. Most 210 s calibrated have FWHM around 125 ps. The 110 s are around 100 ps, but those that incorporate a Zener diode are typically a bit narrower and cluster around

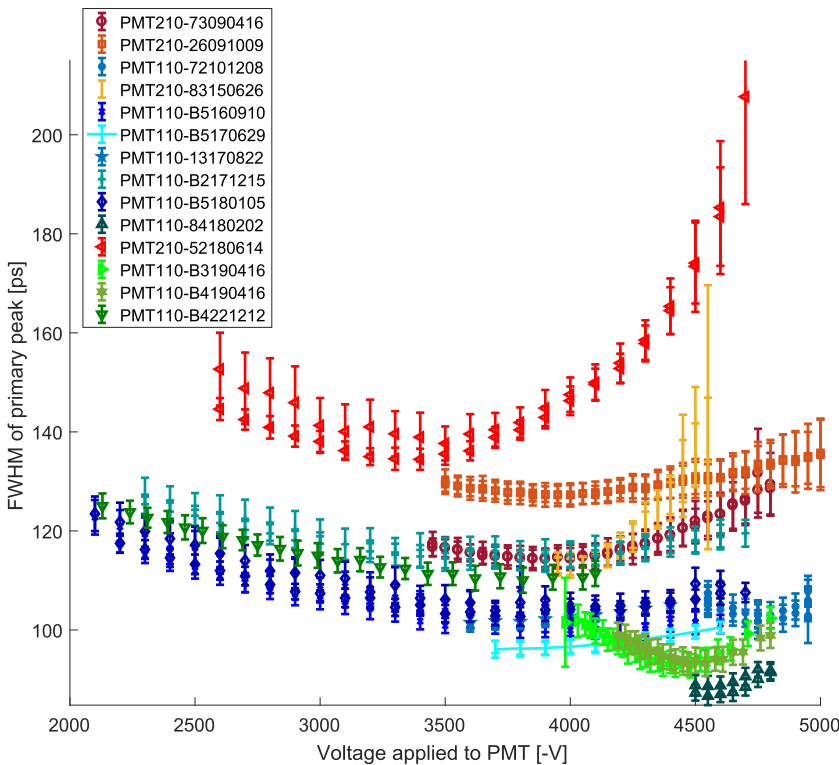


FIG. 3. Data of the FWHM of the primary peak across all the PMTs calibrated. The red and yellow shades are for the two MCP-stage type, while the blue and green shades are for the single MCP types.

90 ps. The variation observed for the FWHM of the IRF for a single bias setting is a few picoseconds. For most non-Zener PMTs, the FWHM change across the nominal (near max) bias voltages is quite flat—seeing a change of a few picoseconds.

For low gain values, the FWHM becomes wider, around 10% or 20% compared to the higher biases. A hypothesis is that at lower biases and gains, the velocity of the electrons avalanching through the MCP is slower, increasing the net transit time through the pores and, therefore, increasing the IRF width. Another hypothesis is that the electron density, which increases by a factor of 10^6 across the bias range, could be substantial enough that space charge contributes and broadens the signal.

The dependence of the gain as a function of the applied bias voltage is shown in Fig. 4. The PMT210 s all have gains near 10^6 and the PMT110 s have max gains near 10^4 . Many of the PMT110 have very similar slopes and values across the bias voltages. The Zener diodes have a notably sharper gain slope. The PMT210s for the most part each have differing slopes. At lower bias settings, the gain falls off at a faster rate.

The dependence of the stability, defined as the variation in the observed integral of the signal, as a function of applied bias, is shown in Fig. 5. The three most recent PMTs do not have directly comparable stability data. One PMT, 110-B5160910, is excluded from the plot because it had massive variation, around 90%, likely signifying that the PMT had some sort of damage, even though the FWHM variation looked nominal. Because the laser energy data were only taken as averages, one cannot distinguish between the variation in the laser

power shot-to-shot or applied PMT gain shot-to-shot. The highest gain values received a few 100 s of unamplified photo-electrons, giving a statistical variation of a few percent. For all lower gain values, the statistics of incoming photons and photo-electrons become negligible. The variation in the applied bias is around ± 2 V, which is negligible in terms of the amplification as well. Higher gain values observe higher variation, but all PMTs sit between 5 and 25%. These data are consistent with that observed in operation on NIF shots. The absolute value of the observed signals on the GRH is used to determine physical values, such as shell areal density³² and total fusion yield.^{33,34} Repeated measurements or multiple measurements of the same signal observe absolute signal value variation within a few tens of percentages. According to the PMT calibration data, the stability is improved at lower gain values, staying within 10%–15%. For a lower applied bias voltage, the relative electron acceleration is decreased throughout the MCP, thereby decreasing the electron avalanche gain per MCP interaction. Because of the decreased average avalanche, both the gain and the variation in the applied gain are likely reduced. The Zener PMTs have notably improved stability, clustering around 4%–7%.

Another metric of interest, specifically for the QCD diagnostic, is the timing delta between when a signal is incident onto the PMT and when the voltage is read out. One PMT (110-B4221212) measured the timing delta shift as a function of bias voltage by using a reference pulse. High gain settings see a minor shift, about 30 ps from peak bias (4.1 kV) to a kV lower (3.1 kV). However, continuing to lower bias voltages leads to an increase in the peak

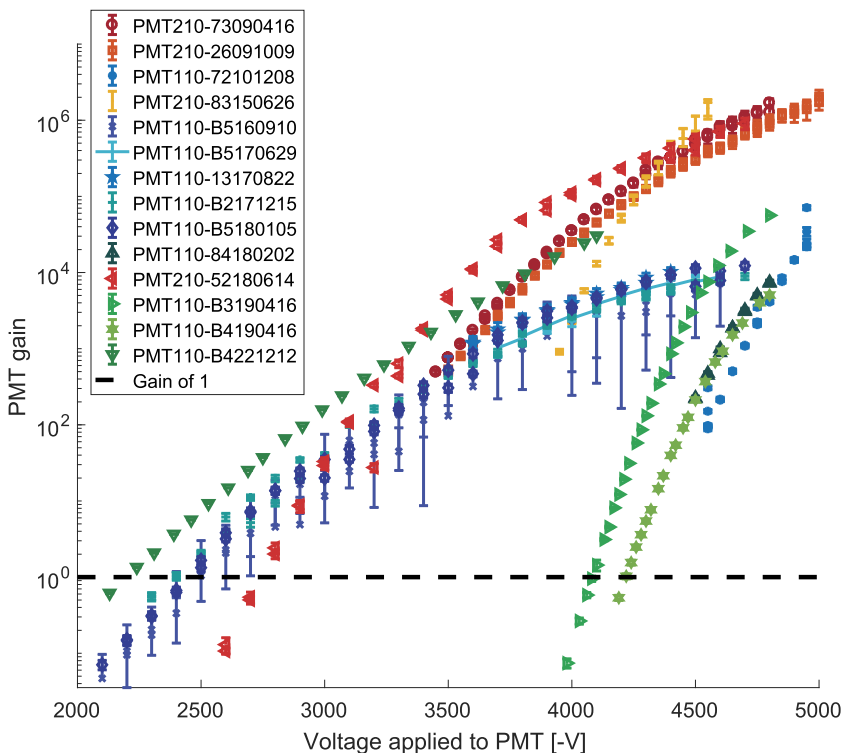


FIG. 4. Data of the observed gain, calculated from the ratio of the integral of the signal to the energy of the laser incident on a log scale. The red and yellow shades are for the two MCP-stage type, while the blue and green shades are for the single MCP types.

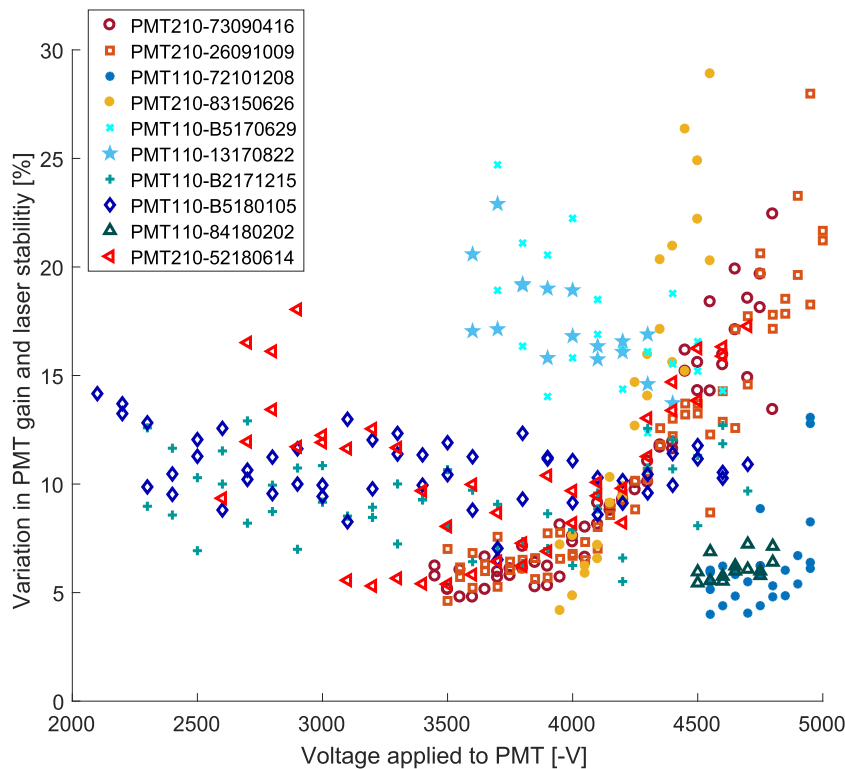


FIG. 5. Data of the observed stability, defined as the standard deviation of the ratio of the integral of the PMT signal and the average incident laser energy. The red and yellow shades are for the two MCP-stage type, while the blue and green shades are for the single MCP types. Because only the average laser energy was recorded, the variation could be attributed to laser or PMT variation. PMT110-B5160910 is excluded because it had values around 0.9, much larger than other PMTs. The three most recent PMTs did not comparably measure stability and so were not included.

shift. At a bias of 2.6 kV, there is a 130 ps shift compared to the max bias. This increase in peak shift for low biases should be considered for timing comparisons between signals that are taken at high and low biases.

This calibration dataset did not explore the dependence of gain, FWHM, and stability relative to charge depletion as the ladder method used kept most data around $1 \text{ V} \cdot \text{ns} = 20 \text{ pC}$. One set of data on PMT110-72101208 collected data with signal strengths from $0.07 \text{ V} \cdot \text{ns}$ (1.4 pC) to $7.5 \text{ V} \cdot \text{ns}$ (150 pC). This collection range is understood to be within the linear regime of the PMT, as typical charge depletion occurs around $60 \text{ V} \cdot \text{ns}$ (1.2 nC).²⁰ Within this charge range, there was no correlation between the charge collected and FWHM of the peak, gain, variation in the peak FWHM, and gain variation, as all data points were within the observed variation at $\sim 1 \text{ V} \cdot \text{ns}$.

IV. EFFECT OF IRFS ON NUCLEAR BURNWIDTHS

A. Single example

Historically, an average PMT IRF was used for analysis, which was taken as an average across the nominal PMT gain settings. In these gain ranges, for most PMTs, the IRF values were taken to be relatively flat and so one representative IRF was used.

Between 2011 and 2022, the yields of ICF implosions on NIF were below 2×10^{16} fusions per implosion. However, since achieving ignition, NIF has produced yields at 2×10^{18} , requiring low gain and bias settings. In a burning plasma with high ($>5 \times 10^{16}$) yields,

the burnwidth becomes narrower,¹⁰ typically smaller than the IRF of the PMT. Therefore, the sensitivity of the IRF used is further compounded. First, we consider one example where the effect of the IRF due to the low gain settings is important.

One NIF implosion achieved a fusion yield of 7.6×10^{17} (2.1 MJ). GRH measured the DT fusion gamma-ray time evolution with Cell C, using PMT110-B5180105 with the applied bias on the PMT of 3.3 kV, quite lower than the max bias of 4.7 kV. The measured signal has an FWHM of 124 ps and is shown in Fig. 6.

At these yields, the burnwidth is so narrow that the deconvolution analysis routine is unsuccessful and returns a flat value that is insensitive to the width of the measured value below a certain value. Either IRF used, gain-dependent or averaged, returns a deconvolution width of 150 ps. The standard, representative PMT IRF has an FWHM of 110.5 ps. When using that IRF, the deconvolution routine finds a burnwidth of 149 ps, while the forward fit routine finds a 74.5 ps burnwidth. However, using a gain-dependent IRF at a bias of 3.3 kV, the PMT IRF has instead an FWHM of 101 ps. Using this more specific, low gain value returns a forward fit value of burnwidths of 85 ps. This 10 ps difference is a 15% difference.

For comparison, the pulse-dilation PMT with a 10 ps resolution, running on the same implosion, observed an FWHM of 90 ± 10 ps. Using the average PMT IRF remains outside the uncertainty while using the low gain IRF is within the expected uncertainty, suggesting that using the low bias specific PMT IRF is closer to the actual value.

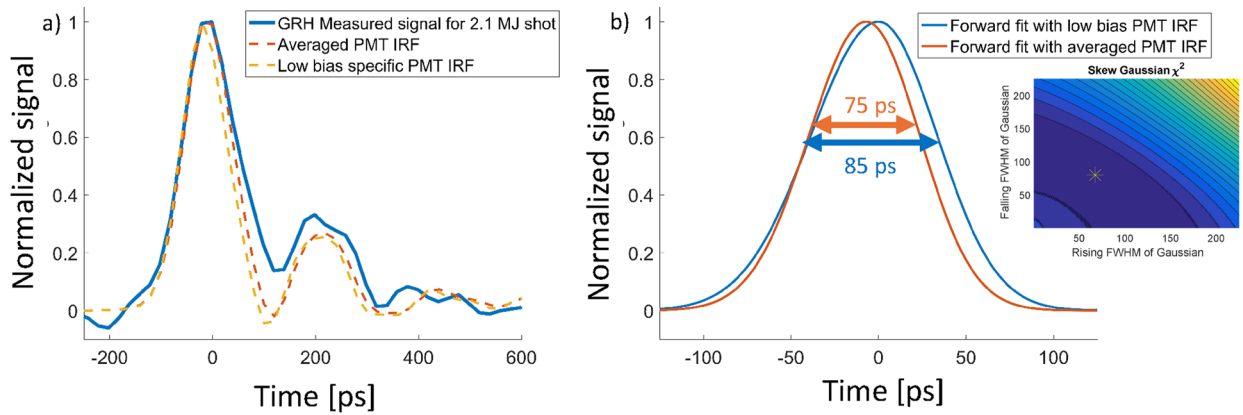


FIG. 6. Example of a very narrow measurement (burnwidth independently measured 90 ± 7 ps with the pulse dilation system) using either the average, nominal PMT IRF or the low bias-specific PMT IRF. (a) The raw measured signal and the two PMT IRFs. (b) The found optimal forward fits with a 10 ps difference, along with the output of a forward fit sensitivity.

B. Effect across ensemble data

For a more aggregate understanding of the importance and relevance of considering gain-dependent IRFs, a dataset of 75 NIF ICF implosions is considered from October 2018 to August 2021. These implosions span a wide range of implosions types,

including CH ablator capsules,³⁵ high-density carbon capsules,^{36,37} Bigfoot implosions,³⁸ alpha heating implosions,^{39,40} pushed single shells,⁴¹ hybrid E implosions,⁴² and direct drive exploding pushers.⁴³ Across this time, one cell of the GRH (Cell A with PMT210-83150626) had a significantly wide IRF (FWHM at max bias: 136 ps).

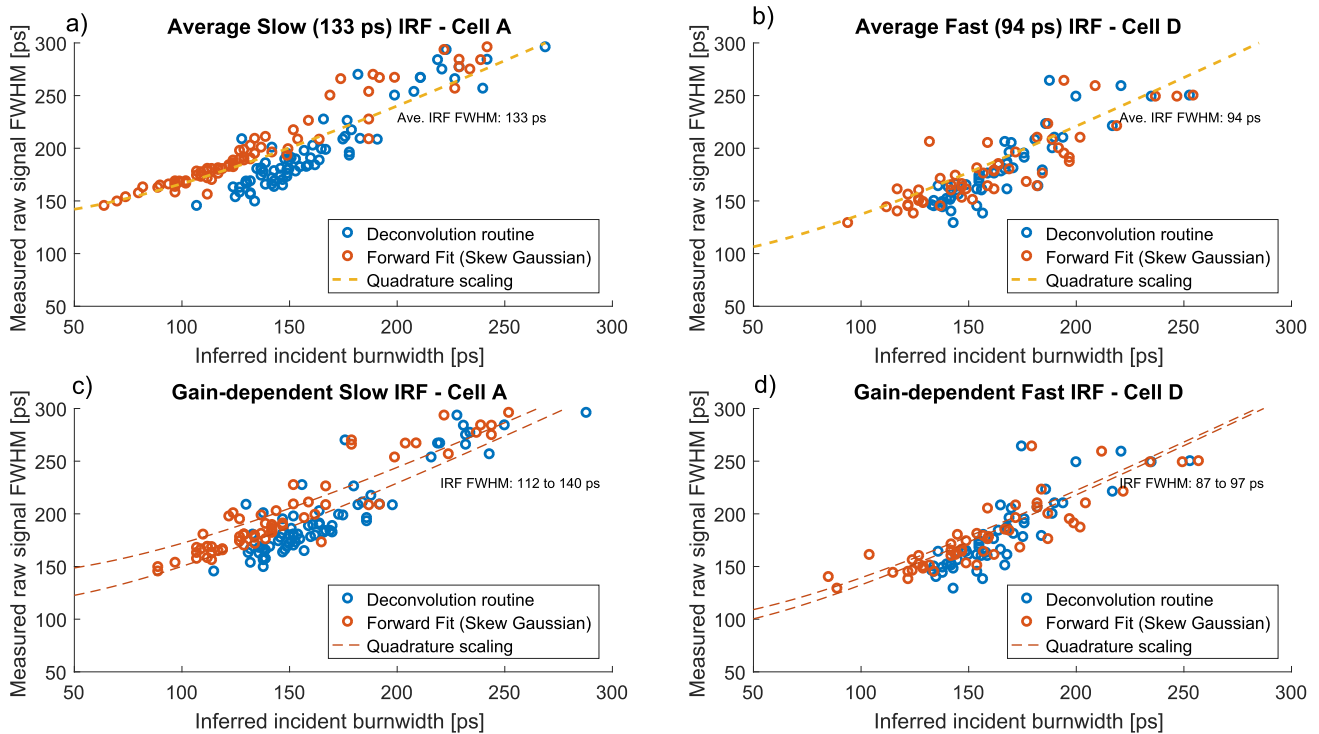


FIG. 7. An ensemble of 75 ICF reaction history values. The same measurement was taken with both (a) and (c) with a slow (133 ps) IRF and (b) and (d) with a fast (94 ps) IRF. The measurements were analyzed using either (a) and (b) an averaged IRF across all values or (c) and (d) a gain-dependent IRF.

In comparison, a second cell (Cell D with PMT110-84180202) measured the same fusion reaction history signal on most implosions, but it had a significantly narrower IRF (FWHM at max bias: 92 ps) due to the Zener diode. Although this dataset, pre-ignition, does not include extremely low bias settings, these two cases provide a contrast between a wide PMT IRF that has a strong gain dependence compared to a Zener diode that is narrow and has less of a bias dependence.

First, consider the burnwidth value found by using an averaged PMT IRF. Figure 7 shows the raw signal and the resulting inferred burnwidth. For Cell A, in Fig. 7(a), because of the wide IRF, one can see that the deconvolution systematically finds a much wider burnwidth value than the forward fit, which follows quite closely the quadrature scaling of the average PMT. Furthermore, the difference between the deconvolution and forward fit is large, with the forward fit finding on average a 26 ps narrower peak (stdev 19 ps). The deconvolution also levels off at widths approximately at the IRF, giving an incident burnwidth value of ~ 130 ps for any measured signal of 165 ps and narrower, while the forward fit continues to infer narrower values. For larger signals, both the forward fit and the deconvolution have a scatter, likely due to wider pulses being significantly non-Gaussian. As a contrast, compare Cell D in Fig. 7(b), with a narrower IRF, where both the deconvolution and the forward fit report values quite similar to each other, with the difference between them being an average of 2 ps (stdev 20 ps).

However, the burnwidth values found with the narrow PMT IRF in Cell D agree closely with the deconvolution values found with the slow PMT in Cell A, as opposed to the forward fit. The burnwidth values the fast PMT IRF finds are on average 7 ps (stdev 18 ps) larger compared to the deconvolution values, which are 36 ps larger (stdev 21 ps) than the forward fit values. This suggests that the forward fit values found with the slow PMT are artificially too narrow, disagreeing with the three other analysis methods.

Now, consider the results when using the gain-dependent IRF values, shown in Fig. 7(c) for the slow PMT and in Fig. 7(d) for the fast PMT. The routine now pulls the IRF for the specific gain value used for the specific shot, thereby varying from 112 to 140 ps for the slow PMT and from 87 to 97 ps for the fast PMT. For the slow PMT Fig. 7(c), the gain-dependent IRF on average gives a deconvolution 6 ps wider (stdev 6 ps) and the forward fit 13 ps wider (stdev 12 ps). Using the gain-dependent IRFs shrinks the difference between the forward fit and deconvolution for the slow PMT, seeing instead a difference of 19 ps (stdev 16 ps). Expectantly, because the fast PMT varies less as a function of bias, the effects of including the gain-dependent IRF are basically negligible, seeing only a 1 ps difference (stdev 10 ps) from the found forward fit and deconvolution values found using the average IRF. Using the gain-dependent IRFs, both the forward fit and deconvolution analysis techniques applied to both Cell A and D measurements give a range of burnwidth values of, on average, 19 ps (stdev 15 ps).

In summary, the ensemble data show that fast PMT IRFs give a tighter range of inferring incident signals. Using bias-dependent IRFs is of especially high importance for slower PMTs and PMTs with high IRF variation—for the case considered here, it changed inferred burnwidths by 13 ps on average, with about a 10% effect. These calibrations will be used to employ gain-dependent IRFs going forward, as well as they motivate upgrading to all narrow

(likely Zener-based) PMTs to improve the data quality and reduce burnwidth uncertainties.

V. CONCLUSION

The nuclear burnwidth is a valuable diagnostic signature for ICF implosions, but challenging to measure because of the short time scale. For the GRH, when the burnwidth is similar to the IRF of the PMT, an analysis routine must be used to remove the effect of the broadening from the PMT.

To understand the dependencies of the PMT, short pulse laser data measuring the FWHM and gain for a set of 15 fast PMTs, six of which measured significantly lower gains was collected. Four of these were Photek210s, which have two stages of multichannel plates and higher gain. The FWHM of the IRF increases at low bias settings and the gain continues to decrease exponentially to low biases.

Historically, an averaged PMT IRF based on the nominal, high gain values was used for the deconvolution and forward fit routine. Using these PMT calibration values to complete analysis routines with a gain-dependent IRF demonstrates better agreement across measurements, reduces the differences between the deconvolution and forward fit, and demonstrates a better agreement when a faster measurement is also collected. Using a gain-dependent IRF has nearly no effect or up to a 15% effect. Going forward, gain-dependent IRFs will be used instead of averaged values. The analysis further emphasizes the benefits of selecting fast IRFs.

ACKNOWLEDGMENTS

This work was supported by the U.S. Department of Energy through the Los Alamos National Laboratory and Lawrence Livermore National Laboratory. Los Alamos National Laboratory is operated by Triad National Security, LLC, for the National Nuclear Security Administration of the U.S. Department of Energy (Contract No. 89233218CNA000001). Lawrence Livermore National Laboratory is supported under Contract No. DE-AC52-07NA2734.

AUTHOR DECLARATIONS

Conflict of Interest

As a conflict of interest notification, note that two authors, J. Milnes and P. Hink, are employees for Photek Ltd., which sells Photek PMTs.

Author Contributions

K. D. Meaney: Conceptualization (equal); Data curation (equal); Formal analysis (equal); Investigation (equal); Writing – original draft (equal); Writing – review & editing (equal). **J. Jeet:** Conceptualization (equal); Data curation (equal); Investigation (equal); Writing – review & editing (equal). **J. Carrera:** Investigation (equal); Methodology (equal). **E. Mariscal:** Investigation (equal); Methodology (equal). **D. Schlossberg:** Investigation (equal); Project administration (equal). **A. Moore:** Investigation (equal). **M. Eckart:** Investigation (equal). **J. Milnes:** Conceptualization (equal); Writing – review & editing (equal). **P. Hink:** Conceptualization (equal);

Writing – review & editing (equal). **P. Hillyard**: Data curation (equal); Investigation (equal); Methodology (equal). **D. Holdener**: Data curation (equal); Investigation (equal); Methodology (equal). **H. Herrmann**: Conceptualization (equal); Data curation (equal); Project administration (equal). **H. Geppert-Kleinrath**: Conceptualization (equal); Investigation (equal). **Y. Kim**: Conceptualization (equal); Funding acquisition (equal); Investigation (equal); Project administration (equal); Supervision (equal).

DATA AVAILABILITY

The data that support the findings of this study are available from the corresponding author upon reasonable request.

REFERENCES

- O. A. Hurricane, D. A. Callahan, P. T. Springer, M. J. Edwards, P. Patel, K. Baker, D. T. Casey, L. Divol, T. Döppner, D. E. Hinkel, L. F. Berzak Hopkins, A. Kritcher, S. Le Pape, S. Maclaren, L. Masse, A. Pak, L. Pickworth, J. Ralph, C. Thomas, A. Yi, and A. Zylstra, “Beyond alpha-heating: Driving inertially confined fusion implosions toward a burning-plasma state on the national ignition facility,” *Plasma Phys. Controlled Fusion* **61**, 014033 (2018).
- O. A. Hurricane, S. A. Maclaren, M. D. Rosen, J. H. Hammer, P. T. Springer, and R. Betti, “A thermodynamic condition for ignition and burn-propagation in cryogenic layer inertially confined fusion implosions,” *Phys. Plasmas* **28**, 022704 (2021).
- A. Pak, L. Divol, C. R. Weber, L. B. Hopkins, D. S. Clark, E. L. Dewald, D. N. Fittinghoff, V. Geppert-Kleinrath, M. Hohenberger, S. Le Pape, T. Ma, A. G. MacPhee, D. A. Mariscal, E. Marley, A. S. Moore, L. A. Pickworth, P. L. Volegov, C. Wilde, O. A. Hurricane, and P. K. Patel, “Impact of localized radiative loss on inertial confinement fusion implosions,” *Phys. Rev. Lett.* **124**, 145001 (2020).
- B. Cheng and P. A. Bradley, “A physical metric for inertial confinement fusion capsules,” *Plasma* **7**, 146–159 (2024).
- B. Cheng, T. J. T. Kwan, Y. M. Wang, F. E. Merrill, C. J. Cerjan, and S. H. Batha, “Analysis of NIF experiments with the minimal energy implosion model,” *Phys. Plasmas* **22**, 082704 (2015).
- B. Cheng, P. A. Bradley, S. M. Finnegan, and C. A. Thomas, “Fundamental factors affecting thermonuclear ignition,” *Nucl. Fusion* **61**, 096010 (2021).
- R. Betti, P. Y. Chang, B. K. Spears, K. S. Anderson, J. Edwards, M. Fatenejad, J. D. Lindl, R. L. McCrory, R. Nora, and D. Shvarts, “Thermonuclear ignition in inertial confinement fusion and comparison with magnetic confinement,” *Phys. Plasmas* **17**, 058102 (2010).
- B. M. Haines, K. D. Meaney, J. J. Kuczek, B. J. Albright, W. S. Daughton, N. M. Hoffman, R. S. Lester, and J. P. Sauppe, “Simulated signatures of ignition,” *Phys. Plasmas* **31**, 042705 (2024).
- H. W. Herrmann, N. Hoffman, D. C. Wilson, W. Stoeffl, L. Dauffy, Y. H. Kim, A. McEvoy, C. S. Young, J. M. Mack, C. J. Horsfield, M. Rubery, E. K. Miller, and Z. A. Ali, “Diagnosing inertial confinement fusion gamma ray physics (invited),” *Rev. Sci. Instrum.* **81**, 10D333 (2010).
- Y. Kim, K. D. Meaney, H. Geppert-Kleinrath, H. W. Herrmann, T. J. Murphy, C. S. Young, N. M. Hoffman, H. J. Jorgenson, T. Morrow, D. C. Wilson, E. N. Loomis, C. Cerjan, A. B. Zylstra, J. Jeet, D. J. Schlossberg, M. S. Rubery, A. S. Moore, A. L. Kritcher, J. A. Carrera, E. F. Mariscal, D. T. Casey, E. L. Dewald, A. E. Leatherland, R. M. Malone, and M. I. Kaufman, “Measurements of fusion reaction history in inertially confined burning plasmas,” *Phys. Plasmas* **30**, 072706 (2023).
- Y. Kim and H. W. Herrmann, “Gamma-ray measurements for inertial confinement fusion applications,” *Rev. Sci. Instrum.* **94**, 041101 (2023).
- B. Leskovar, “Microchannel plates,” *Phys. Today* **30**(11), 42–49 (1977).
- J. L. Wiza, “Microchannel plate detectors,” *Nucl. Instrum. Methods* **162**, 587–601 (1979).
- S. Dhawan, “Introduction to microchannel plate photomultipliers,” *IEEE Trans. Nucl. Sci.* **28**, 672–676 (1981).
- J. S. Milnes and J. Howorth, “Picosecond time response characteristics of microchannel plate PMT detectors,” in *26th International Congress on High-Speed Photography and Photonics, International Society for Optics and Photonics*, edited by D. L. Paisley, S. Kleinfelder, D. R. Snyder and B. J. Thompson (SPIE, 2005), Vol. 5580, pp. 730–740.
- J. R. Howorth, J. S. Milnes, C. J. Horsfield, and J. M. Mack, “Ultra-fast photomultipliers with high dynamic range,” in HSPF Conference, 2006.
- J. Howorth, I. Cox, J. Milnes, and G. Jones, “Recent improvements in photomultipliers and read-out systems,” in *Detectors and Imaging Devices: Infrared, Focal Plane, Single Photon, International Society for Optics and Photonics*, edited by E. L. Dereniak, J. P. Hartke, P. D. LeVan, R. E. Longshore, A. K. Sood, and M. Razeghi (SPIE, 2010), Vol. 7780, p. 77800X.
- J. Milnes, “Recent developments in ultra-high speed and large area photomultiplier tubes,” in *1st EPS Conference on Plasma Diagnostics (ECPD2015)* (ECPD, 2016), p. 5.
- J. S. Milnes, C. J. Horsfield, M. S. Rubery, V. Y. Glebov, and H. W. Herrmann, “Ultra-high speed photomultiplier tubes with nanosecond gating for fusion diagnostics,” *Rev. Sci. Instrum.* **83**, 10D301 (2012).
- J. S. Milnes, T. M. Conneely, and C. J. Horsfield, “Analogue saturation limit of single and double 10 mm microchannel plate photomultiplier tubes,” *Rev. Sci. Instrum.* **87**, 11D832 (2016).
- K. D. Meaney, S. Kerr, G. J. Williams, H. Geppert-Kleinrath, Y. Kim, H. W. Herrmann, D. H. Kalantar, A. Mackinnon, M. Bowers, L. Pelz, D. Alessi, D. Martinez, M. Prantl, S. Herriot, M. R. Hermann, T. E. Lanier, M. Hamamoto, J. M. Di Nicola, S. Yang, W. Williams, C. Widmayer, and R. Lowe-Webb, “Multi-pulse time resolved gamma ray spectroscopy of the advanced radiographic capability using gas Cherenkov diagnostics,” *Phys. Plasmas* **28**, 033102 (2021).
- V. Y. Glebov, C. Stoeckl, C. J. Forrest, J. P. Knauer, O. M. Mannion, M. H. Romanofsky, T. C. Sangster, and S. P. Regan, “A novel photomultiplier tube neutron time-of-flight detector,” *Rev. Sci. Instrum.* **92**, 013509 (2021).
- J. M. Gordon, D. J. Schlossberg, M. J. Eckart, P. S. Datte, C. E. Durand, G. P. Grim, E. P. Hartouni, R. Hatarik, and A. S. Moore, “Characterization of photodetector temporal response for neutron time-of-flight (nToF) diagnostics at the National Ignition Facility,” *Rev. Sci. Instrum.* **89**, 10I135 (2018).
- D. J. Schlossberg, G. P. Grim, D. T. Casey, A. S. Moore, R. Nora, B. Bachmann, L. R. Benedetti, R. M. Bionta, M. J. Eckart, J. E. Field, D. N. Fittinghoff, M. Gatut Johnson, V. Geppert-Kleinrath, E. P. Hartouni, R. Hatarik, W. W. Hsing, L. C. Jarrott, S. F. Khan, J. D. Kilkenny, O. L. Landen, B. J. MacGowan, A. J. Mackinnon, K. D. Meaney, D. H. Munro, S. R. Nagel, A. Pak, P. K. Patel, B. K. Spears, P. L. Volegov, and C. V. Young, “Observation of hydrodynamic flows in imploding fusion plasmas on the national ignition facility,” *Phys. Rev. Lett.* **127**, 125001 (2021).
- H. Abu-Shawareb and Indirect Drive ICF Collaboration, “Lawson criterion for ignition exceeded in an inertial fusion experiment,” *Phys. Rev. Lett.* **129**, 075001 (2022).
- H. Abu-Shawareb and The Indirect Drive ICF Col, and laboration, “Achievement of target gain larger than unity in an inertial fusion experiment,” *Phys. Rev. Lett.* **132**, 065102 (2024).
- M. E. Guillaume and N. S. Nauhman, *Deconvolution of Time Domain Wavefunctions in the Presence of Noise* (National Bureau of Standards, 1981).
- J. Andrews, “Deconvolution of system impulse responses and time domain waveforms,” Technical Report (Picosecond Pulse Lab, 2004) application Note AN-18.
- H. Geppert-Kleinrath, H. W. Herrmann, Y. H. Kim, A. B. Zylstra, K. Meaney, F. E. Lopez, B. J. Pederson, J. Carrera, H. Khater, C. J. Horsfield, M. S. Rubery, S. Gales, A. Leatherland, A. Meadowcroft, T. Hilsabeck, J. D. Kilkenny, R. M. Malone, J. D. Hares, A. K. L. Dymoke-Bradshaw, J. Milnes, and C. McFee, “Pulse dilation gas Cherenkov detector for ultra-fast gamma reaction history at the NIF (invited),” *Rev. Sci. Instrum.* **89**, 10I146 (2018).
- S. G. Gales, C. J. Horsfield, A. L. Meadowcroft, A. E. Leatherland, H. W. Herrmann, J. D. Hares, A. K. L. Dymoke-Bradshaw, J. S. Milnes, Y. H. Kim, H. G. Kleinrath, K. Meaney, A. B. Zylstra, S. Parker, D. Hussey, L. Wilson, S. F. James, J. D. Kilkenny, and T. J. Hilsabeck, “Characterisation of a sub-20 ps temporal resolution pulse dilation photomultiplier tube,” *Rev. Sci. Instrum.* **89**, 063506 (2018).

- ³¹The PMT serial ID used is in the form PMTx10-xxYYMMDD, where 210 vs 110 refers to a two stage of one stage MCPs, the xx is a specific serial number and the remaining numbers refer to the year, month and day of fabrication of the PMT.
- ³²K. D. Meaney, Y. H. Kim, H. W. Herrmann, H. Geppert-Kleinrath, and N. M. Hoffman, "Improved inertial confinement fusion gamma reaction history 12C gamma-ray signal by direct subtraction," *Rev. Sci. Instrum.* **90**, 113503 (2019).
- ³³K. D. Meaney, Y. Kim, H. Geppert-Kleinrath, H. W. Herrmann, A. S. Moore, E. P. Hartouni, D. J. Schlossberg, E. Mariscal, J. Carrera, and J. A. Church, "Total fusion yield measurements using deuterium-tritium gamma rays," *Phys. Plasmas* **28**, 102702 (2021).
- ³⁴Y. Kim, J. M. Mack, H. W. Herrmann, C. S. Young, G. M. Hale, S. Caldwell, N. M. Hoffman, S. C. Evans, T. J. Sedillo, A. McEvoy, J. Langenbrunner, H. H. Hsu, M. A. Huff, S. Batha, C. J. Horsfield, M. S. Rubery, W. J. Garbett, W. Stoeffl, E. Grafil, L. Bernstein, J. A. Church, D. B. Sayre, M. J. Rosenberg, C. Waugh, H. G. Rinderknecht, M. Gatu Johnson, A. B. Zylstra, J. A. Frenje, D. T. Casey, R. D. Petrasso, E. K. Miller, V. Y. Glebov, C. Stoeckl, and T. C. Sangster, "Determination of the deuterium-tritium branching ratio based on inertial confinement fusion implosions," *Phys. Rev. C* **85**, 061601 (2012).
- ³⁵A. L. Kritcher, D. Clark, S. Haan, S. A. Yi, A. B. Zylstra, D. A. Callahan, D. E. Hinkel, L. F. Berzak Hopkins, O. A. Hurricane, O. L. Landen, S. A. MacLaren, N. B. Meezan, P. K. Patel, J. Ralph, C. A. Thomas, R. Town, and M. J. Edwards, "Comparison of plastic, high density carbon, and beryllium as indirect drive NIF ablaters," *Phys. Plasmas* **25**, 056309 (2018).
- ³⁶L. B. Hopkins, S. LePape, L. Divol, A. Pak, E. Dewald, D. D. Ho, N. Meezan, S. Bhandarkar, L. R. Benedetti, T. Bunn, J. Biener, J. Crippen, D. Casey, D. Clark, D. Edgell, D. Fittinghoff, M. Gatu-Johnson, C. Goyon, S. Haan, R. Hatarik, M. Havre, D. Hinkel, H. Huang, N. Izumi, J. Jaquez, O. Jones, S. Khan, A. Kritcher, C. Kong, G. Kyrala, O. Landen, T. Ma, A. MacPhee, B. MacGowan, A. J. Mackinnon, M. Marinak, J. Milovich, M. Millot, P. Michel, A. Moore, S. R. Nagel, A. Nikroo, P. Patel, J. Ralph, H. Robey, J. S. Ross, N. G. Rice, S. Sepke, V. A. Smalyuk, P. Sterne, D. Strozzi, M. Stadermann, P. Volegov, C. Weber, C. Wild, C. Yeamans, D. Callahan, O. Hurricane, R. P. J. Town, and M. J. Edwards, "Toward a burning plasma state using diamond ablator inertially confined fusion (ICF) implosions on the national ignition facility (NIF)," *Plasma Phys. Controlled Fusion* **61**, 014023 (2018).
- ³⁷D. S. Clark, D. T. Casey, C. R. Weber, O. S. Jones, K. L. Baker, E. L. Dewald, L. Divol, A. Do, A. L. Kritcher, O. L. Landen, M. Millot, J. L. Milovich, V. A. Smalyuk, D. J. Strozzi, A. E. Pak, R. Tommasini, and M. J. Edwards, "Exploring implosion designs for increased compression on the National Ignition Facility using high density carbon ablaters," *Phys. Plasmas* **29**, 052710 (2022).
- ³⁸D. T. Casey, C. A. Thomas, K. L. Baker, B. K. Spears, M. Hohenberger, S. F. Khan, R. C. Nora, C. R. Weber, D. T. Woods, O. A. Hurricane, D. A. Callahan, R. L. Berger, J. L. Milovich, P. K. Patel, T. Ma, A. Pak, L. R. Benedetti, M. Millot, C. Jarrott, O. L. Landen, R. M. Bionta, B. J. MacGowan, D. J. Strozzi, M. Stadermann, J. Biener, A. Nikroo, C. S. Goyon, N. Izumi, S. R. Nagel, B. Bachmann, P. L. Volegov, D. N. Fittinghoff, G. P. Grim, C. B. Yeamans, M. Gatu Johnson, J. A. Frenje, N. Rice, C. Kong, J. Crippen, J. Jaquez, K. Kangas, and C. Wild, "The high velocity, high adiabat, "Bigfoot" campaign and tests of indirect-drive implosion scaling," *Phys. Plasmas* **25**, 056308 (2018).
- ³⁹K. L. Baker, O. Jones, C. Weber, D. Clark, P. K. Patel, C. A. Thomas, O. L. Landen, R. Nora, G. J. Anderson, J. Gaffney, S. MacLaren, D. T. Casey, T. Döppner, E. L. Dewald, R. Tommasini, B. K. Spears, J. Salmonson, M. Hohenberger, S. Khan, A. Zylstra, A. Kritcher, P. Amendt, V. Smalyuk, J. Lindl, C. Young, J. S. Ross, D. Ho, O. A. Hurricane, D. A. Callahan, T. Woods, J. L. Milovich, D. J. Strozzi, B. Bachmann, R. Bionta, P. M. Celliers, D. Fittinghoff, R. Hatarik, M. Gatu Johnson, K. Meaney, M. Millot, P. L. Volegov, and C. Wilde, "Hydroscaling indirect-drive implosions on the national ignition facility," *Phys. Plasmas* **29**, 062705 (2022).
- ⁴⁰K. L. Baker, S. MacLaren, O. Jones, B. K. Spears, P. K. Patel, R. Nora, L. Divol, O. L. Landen, G. J. Anderson, J. Gaffney, M. Kruse, O. A. Hurricane, D. A. Callahan, A. R. Christopherson, J. Salmonson, E. P. Hartouni, T. Döppner, E. Dewald, R. Tommasini, C. A. Thomas, C. Weber, D. Clark, D. T. Casey, M. Hohenberger, S. Khan, T. Woods, J. L. Milovich, R. L. Berger, D. Strozzi, A. Kritcher, B. Bachmann, R. Benedetti, R. Bionta, P. M. Celliers, D. Fittinghoff, R. Hatarik, N. Izumi, M. Gatu Johnson, G. Kyrala, T. Ma, K. Meaney, M. Millot, S. R. Nagel, A. Pak, P. L. Volegov, C. Yeamans, and C. Wilde, "Alpha heating of indirect-drive layered implosions on the national ignition facility," *Phys. Rev. E* **107**, 015202 (2023).
- ⁴¹E. L. Dewald, J. E. Pino, R. E. Tipton, J. D. Salmonson, J. Ralph, E. Hartouni, S. F. Khan, R. Hatarik, C. V. Young, D. Thorn, V. A. Smalyuk, R. Sacks, A. Nikroo, N. Rice, S. A. MacLaren, S. Prisbrey, B. A. Remington, and F. Graziani, "Pushed single shell implosions for mix and radiation trapping studies using high-Z layers on National Ignition Facility," *Phys. Plasmas* **26**, 072705 (2019).
- ⁴²A. L. Kritcher, A. B. Zylstra, D. A. Callahan, O. A. Hurricane, C. Weber, J. Ralph, D. T. Casey, A. Pak, K. Baker, B. Bachmann, S. Bhandarkar, J. Biener, R. Bionta, T. Braun, M. Bruhn, C. Choate, D. Clark, J. M. Di Nicola, L. Divol, T. Döppner, V. Geppert-Kleinrath, S. Haan, J. Heebner, V. Hernandez, D. Hinkel, M. Hohenberger, H. Huang, C. Kong, S. Le Pape, D. Mariscal, E. Marley, L. Masse, K. D. Meaney, M. Millot, A. Moore, K. Newman, A. Nikroo, P. Patel, L. Pelz, N. Rice, H. Robey, J. S. Ross, M. Rubery, J. Salmonson, D. Schlossberg, S. Sepke, K. Sequoia, M. Stadermann, D. Strozzi, R. Tommasini, P. Volegov, C. Wild, S. Yang, C. Young, M. J. Edwards, O. Landen, R. Town, and M. Herrmann, "Achieving record hot spot energies with large HDC implosions on NIF in HYBRID-E," *Phys. Plasmas* **28**, 072706 (2021).
- ⁴³C. B. Yeamans, G. E. Kemp, Z. B. Walters, H. D. Whitley, P. W. McKenty, E. M. Garcia, Y. Yang, R. S. Craxton, and B.E. Blue, "High yield polar direct drive fusion neutron sources at the National Ignition Facility," *Nucl. Fusion* **61**, 046031 (2021).